https://doi.org/10.1016/j.msea.2024.146111

A study on the microstructure and mechanical behavior of CoCrFeNi high entropy alloy fabricated via laser powder bed fusion: Experiment and crystal plasticity finite element modelling

Yongyun Zhang[1, 2], Congrui Yang[1,2], Haibo Ke[1*], K.C. Chan [2,3*], Weihua Wang[1,4]

1. *Songshan Lake Materials Laboratory, Dongguan 523808, China*
2. *Research Institute for Advanced Manufacturing, Department of Industrial and Systems Engineering, The Hong Kong Polytechnic University*
3. *State Key Laboratory of Ultra-precision Machining Technology, Department of Industrial and Systems Engineering, The Hong Kong Polytechnic University, Hong Kong, China*
4. *Institute of Physics, Chinese Academy of Sciences, Beijing 100190, China*

---

[*] Corresponding author.

E-mail address: (kehaibo@sslab.org.cn)

[*] Corresponding author.

E-mail address: (kc.chan@polyu.edu.hk)

Abstract

Additive manufacturing facilitates the design of high entropy alloys (HEAs) with well-performing properties compared to conventional manufacturing methods. However, a significant obstacle to the industrial application of the equimolar CoCrFeNi HEA fabricated through additive manufacturing is the detrimental impact of thermal cracks on its performance. Here, thermal crack-free CoCrFeNi HEAs with enhanced mechanical properties were obtained by optimizing the energy input in laser powder bed fusion (LPBF). The lower energy input resulted in finer grains, leading to simultaneously improved strength and ductility compared to the one fabricated via higher energy input. To understand the relationship between the microstructure and mechanical properties, crystal plasticity element modelling (CPFEM) was employed to accurately model the experimental results. Using the collected constitutive parameters for CoCrFeNi HEA after CPFEM, in-situ tensile modelling was implemented on a converted orientation map of an as-LPBF CoCrFeNi sample. The CPFEM results reveals that the appearance of deformed twins during the initial plastic deformation stage, attributed to a complex distribution of shear strain on the grain boundaries. The interaction between the deformed twins and dislocation motion emerged as the primary deformation mechanisms in the as-LPBF CoCrFeNi HEA, resulting in complex stress and strain distributions. By combing experimental data with modelling techniques, a viable approach to comprehending the detailed deformation mechanism of deformed twins was established.

Key words: Equimolar CoCrFeNi high entropy alloy; Laser powder bed fusion; Microstructure; Mechanical properties; Crystal Plasticity Element Modelling; Deformation mechanism

1 Introduction

Compared to conventional alloys such as steel and Ti alloys, multi-component alloys, also known as high entropy alloys (HEAs) due to their high mixing entropy [1], generally possess unique properties. These properties include superior strength and ductility [2], as well as excellent oxidation and corrosion resistance [3], making them suitable for a wide range of applications from automobile to aerospace [4]. The equimolar CoCrFeNi HEA with mediocre properties is generally used as the base materials for designing novel HEAs by introducing other alloying elements [5–8]. Traditional design methods for HEAs still rely on the casting [1], but they require additional processes such as homogenization or post-processing approaches [9], as well as the combination of mechanical alloying and spark plasma sintering (SPS) [10] or other powder metallurgy methods [11,12]. These conventional approaches are time-consuming and can lead to issues such as shrinkage cavities [13] in casting or the formation of precipitations [12] in powder metallurgy. However, customizing complex-shaped HEA specimens for industrial applications is a complex procedure, which can be directly achieved by additive manufacturing (AM) methods.

Laser powder bed fusion (LPBF) is a widely used AM technique for fabricating HEAs. Brif et al. [14] first reported the fabrication of CoCrFeNi HEA specimens by LPBF and they found that these samples exhibited higher strength and ductility compared to conventional engineering materials. However, LPBF fabrication of CoCrFeNi HEA has its challenges, as it is prone to hot tearing [15]. This issue often leads to crack formation in the as-LPBF CoCrFeNi HEA specimens, which can be attributed to improper parameters [16]. Additionally, at elevated temperatures, as-LPBF CoCrFeNi specimens suffer from ductility loss due to crack formation along grain boundaries caused by nano-clustering [17]. To address this issue, alloying elements such as Al [18], are added to the CoCrFeNi system to inhibit the formation of hot cracks, so the obtained as-

LBPF $Al_{0.5}CoCrFeNi$ has minimal hot cracks [18]. Despite LPBF-fabricated products are known to process desirable properties compared to the wrought-annealed samples due to their unique structures [19], they often suffer from ductility losses. While optimizing the LPBF parameters can eliminate cracks [16], there is still a significant reduction in ductility (a near-half loss) comparted to as-cast samples [20]. Consequently, post-treatments are employed to improve ductility, such as annealing [21,22] and cold deformation [23], while these treatments can weaken the yield strength of the as-LPBF samples [21,22]. Cold deformation followed by the annealing has been proven to effectively improve mechanical properties of as-LPBF CoCrFeNi products [23]. Nevertheless, the complexity of these processes limits their practical application, highlighting the need for direct parameter optimization to improve the properties of LPBF-fabricated HEAs.

Studying the principles of deformation mechanisms in engineering materials is crucial as it provides valuable guidance for designing high-performing materials. In the case of CoCrFeNi HEA, which has a lower stacking fault energy (SFE) of 32.5 mJ/m^2 [24], deformation triggers twinning-induced plasticity (TWIP) [25]. In-situ experiments, including in situ neutron diffraction [26], electron backscatter diffraction [27,28], synchrotron x-ray diffraction (XRD) [28], etc, can be conducted for studying the microstructural evolution during deformation. Alternatively, simulation methods like crystal plasticity finite modeling (CPFEM) have been used to study the deformation behavior of TWIP steels [29–32]. CPFEM has also been applied to other HEAs, including interstitial HEAs [33,34] and $CoCrFeNiAl_x$ HEAs [35]. For instance, Lu et al. [33] studied the stress level-dependent cyclic plasticity and microstructural evolution using constitutive models derived from the experiments. Zhang et al. [34] also developed a constitutive model to study the effects of temperature and grain size on strengthening and plasticity mechanism in an interstitial HEA, finding that increasing the elements in the representative volume element (RVE) approach improves the calculation accuracy. The strain hardening behavior of CoCrFeNiAl$_x$ HEAs was investigated by the CPFEM method, revealing that Al-doped HEA exhibit a higher strain hardening rate compared to ordinary HEAs without Al [35]. However, these studies rarely address microstructure evolution during deformation, especially for materials fabricated via AM approaches. Diehl et al. [29] introduced an integrated CPFEM approach utilizing RVEs through DREAM.3D [36] and the Düsseldorf Advanced Materials Simulation Kit (DAMASK) [37] package, enabling in-situ tensile modeling based on experimental grain orientation maps for studying the microstructural evolution during deformation.

In our study, the effect of the laser energy inputs on the microstructure and mechanical properties of as-LPBF CoCrFeNi samples was investigated. Thermal crack-free CoCrFeNi HEA samples with improved mechanical properties were successfully fabricated. Based on the observed microstructure in the LBPF-fabricated HEA sample, polycrystalline RVEs with the similar characteristics like grain size and morphologies were used in CPFEM to determine the constitutive parameters for CoCrFeNi HEA. Furthermore, an in-situ tensile CPFEM was realized to study the microstructure evolution during deformation, establishing a correlation between microstructure and macro-deformation behavior. Our study introduces a novel approach to investigating the deformation behavior in multi-component alloys, and integration of experimental data with computational modelling can be extended to a broader range of materials, enhancing predictive capabilities.

2 Methodology

2.1 Material and processing

The gas-atomized equimolar CoCrFeNi HEA powders (VMP Inc., China), with a nominal particle size ranging from 15 μm to 53 μm, were utilized in the LPBF process for specimen fabrication. The powder morphology was observed in scanning electron microscopy (SEM, Sigma 300, Zeiss, Germany), revealing that the spherical HEA powders with a little satellite powder are fabricated by the gas atomization process, as shown in Fig. 1 (a). Fig. 1 (b) displays the particle size distribution obtained using a particle size analyzer (Mastersizer 3000, Malvern, UK), indicating that the powder has a D50 of 30 μm and a D90 of 47 μm. The microstructure of the HEA powder was investigated using SEM equipped with an electron backscatter diffraction (EBSD, C-nano, Oxford Instrument, UK) and energy disperse spectroscopy (EDS, X-Xax, Oxford Instruments, UK) detectors, demonstrating the formation of equiaxed grains (Fig. 1 (c)) with an distribution of alloying elements (Fig. 1 (d)). The HEA specimens were fabricated in a LBPF system (SLM 125 HL, SLM Solutions Group AG, Germany) using a zigzag scanning strategy with a 67 ° rotation in each subsequent building layer. The scanning speed used was 600 mm/s, while the interval and the layer thickness were set at 100 μm and 50 μm, respectively. To investigate the impact of heat input on the microstructure and mechanical properties, the laser power was varied in this study, with values of 225 W and 375 W. Additionally, a pre-heated 304 stainless steel substrate at 150 ℃ was utilized to reduce the residual stress in the LPBF samples [38]. After the fabrication process, the densities of the samples fabricated with different energy inputs were measured using a density balance (Sartorius SQP, Germany) through the drainage method. It was found that both samples had a similar density of approximately 8.18 g/cm^3.

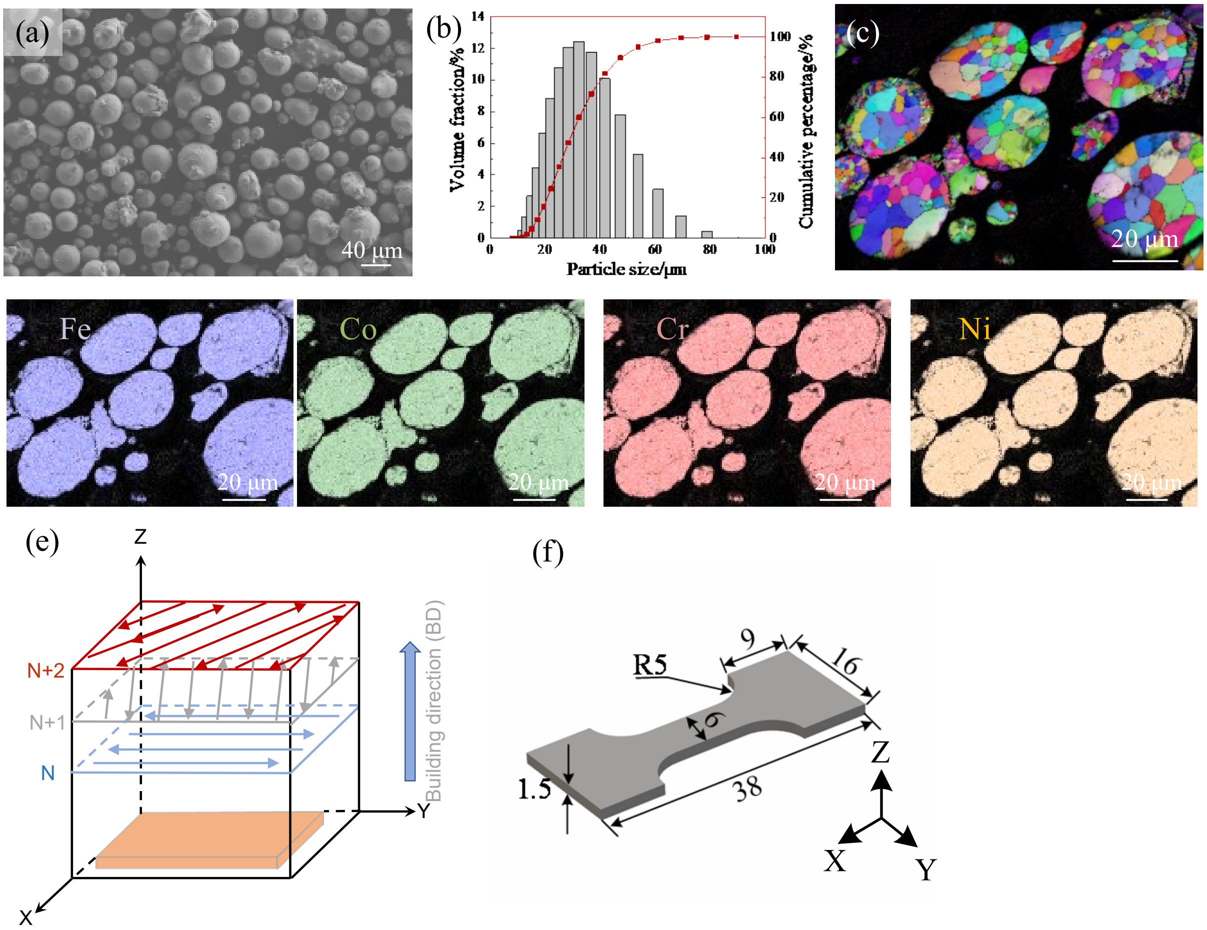

Fig. 1 The CoCrFeNi HEA powder used in the LPBF approach of (a) the morphology in SEM, (b) the particle size distribution, (c) the IPF figure of HEA powders with (d) corresponding EDS element maps; (d) shows the fabrication strategies used in LPBF and (d) the tensile bar schematic diagram used in the tensile test

2.2 Mechanical tests and characterization techniques

The as-LPBF samples, fabricated using laser powers of 225 W (S1) and 375 W (S2), were cut from the 304 stainless steel substrates by an electrical wire cutting machine for subsequent testing. The different planes, including the XY plane perpendicular to building direction (BD) and XY plane parallel to BD, were ground using wet sandpaper with a step-up mesh number to 2000. The well-ground surfaces were then polished using a diamond polishing suspension, followed by the application of oxide particle solution (SiO_2, 50 nm) for EBSD preparation. These planes were observed in an SEM equipped with an EBSD detector at a step size of 2 µm to study the microstructure and the texture evolution after LPBF. X-ray diffraction (XRD, SmartLab, Japan) was performed on the XY surface of S2 with a step size of 0.01°, using a copper target. The sub-micron microstructure of the as-LPBF sample was investigated by transmission electron microscopy (TEM, JEM F200, Japan) on the sample prepared by a precision ion polishing system (PIPS II, 695c, USA). A universal testing machine (TestStar Wance, China) was used for performing the ambient tensile tests with a strain rate of 10^{-3}/s on three samples (as shown in Fig. 1 (e)) to obtain an value property from samples fabricated under different laser powers. The fracture surface structure was observed in SEM while the microstructure in the near-fracture area was examined using EBSD and TEM.

2.3 Constitutive model in CPFEM

2.3.1 Crystal plasticity framework

Based on the seminal work of Asaro and Needleman [39] and Pierce et al. [40], the CPFEM was developed to investigate the deformation mechanisms by incorporating the crystal orientation and activated slip systems. The following equation gives the expression of the total deformation gradient $\boldsymbol{F}$ for finite strain [41]:

$$\boldsymbol{F} = \boldsymbol{F}^e \boldsymbol{F}^p \qquad \text{Eq. 1}$$

where $\boldsymbol{F}^e$ is the elastic-deformation gradient, contributed by elastic stretching etc.; $\boldsymbol{F}^p$ denotes the plastic-deformation gradient arising from slipping, twinning and phase transformation. The plastic velocity gradient tensor, $\boldsymbol{L}^p$, is obtained by summing the shear strain rates ($\dot{\gamma}^{\alpha}$) in all slip systems, as expressed in:

$$\boldsymbol{L^p} = \boldsymbol{F^p}(\boldsymbol{F^p})^{-\boldsymbol{1}} = \sum_{\alpha=1}^{N_s}\dot{\gamma}^{\alpha}\boldsymbol{m}^{\alpha}\otimes\boldsymbol{n}^{\alpha} \qquad \text{Eq. 2}$$

where N_s is the activated slip systems of 12 in FCC materials; $\boldsymbol{m}^{\alpha}$ is the unit vectors along with shear direction on slip system α, while $\boldsymbol{n}^{\alpha}$ is the one along with normal direction. Additionally, the contribution of deformation twining to the factor of $\boldsymbol{L}^p$ is considered and given as follows [42]:

$$\boldsymbol{L^p} = (1-f_{tw})\sum_{\alpha=1}^{N_s}\dot{\gamma}^{\alpha}\boldsymbol{m}^{\alpha}\otimes\boldsymbol{n}^{\alpha} + \sum_{\beta=1}^{N_{tw}}\dot{\gamma}^{\beta}\boldsymbol{m}_{tw}^{\beta}\otimes\boldsymbol{n}_{tw}^{\beta} \qquad \text{Eq. 3}$$

where f_{tw} represents the total volume fraction of the deformed twins; N_{tw}=12 is the number of twin systems.

2.3.2 Dislocation slip

The constitutive model considers both dislocation slip in the non-twinned FCC phase and the plastic strain formed by shear deformation during twinning. To account for these effects, a modified equation based on the Orowan equation [43] is used, which is described as follows [33]:

$$\dot{\gamma}^{\alpha} = \rho^{\alpha}b_s v_0 \exp\left\{-\frac{Q_s}{k_b T}\left[1-\left(\frac{|\tau_s^{\alpha}-\tau_b^{\alpha}|-\tau_p^{\alpha}}{\tau_0}\right)^{p}\right]^{q}\right\} sign(\tau_s^{\alpha}-\tau_b^{\alpha}) \qquad \text{Eq. 4}$$

where ρ^{α} is the current dislocation density of α slip system; b_s is the Burgers vector which equals $\frac{\sqrt{2}a}{2}$ (a is the lattice constant of CoCrFeNi HEA); v_0 is the reference dislocation velocity of 1×10^{-4} m/s given by Lu et al. [30]; Q_s represents the activation energy for the slip of 3.5×10^{-19} J [31]; k_b is Boltzmann constant while T represents temperature in Kelvin; p and q are the parameters related to the obstacle profiles [34]; $\tau_b^{\alpha}, \tau_p^{\alpha}$ represent the backing stress and passing stress, respectively, while τ_0 is the lattice resistance. These terms are used to describe the kinematic and isotropic hardening behavior in the following subsections. It should be noted that τ_0 can be considered constant during deformation. The value of the back stress of τ_b^{α} is determined by the number of dislocation pile-ups (especially on GBs and TBs) in the front of obstacles and is expressed in the following:

$$\tau_b^\alpha = \frac{Gb}{\Lambda_s^\alpha} N^a \left(1 - \frac{N^a}{N^*}\right) \qquad \text{Eq. 5}$$

where G and Λ_s^α are shear moduli of CoCrFeNi alloy and the dislocation mean free path (MFP) [44], respectively; the factor $(1 - \frac{N^a}{N^*})$ represents the screening effect of back stress [45]. To determine the flux of dislocations per slip band that can reach a boundary, the following equation can be utilized:

$$\dot{N}^\alpha = \frac{l}{b}\left(1 - \frac{N^a}{N^*}\right)|\dot{\gamma}^\alpha| \qquad \text{Eq. 6}$$

where l is the average distance between slip bands, while N^* represents the saturated value of piled-up dislocations on the boundaries, which can be assumed as constant during deformation [30]. This is because the number of piled-up dislocations would not increase further once the factor of N^a reached N^*.

The microstructure geometrical length scale Λ_s^α given in Eq. 5 can be defined as a combined effect from grain boundaries (GBs) and twin boundaries (TBs) given in [44]:

$$\frac{1}{\Lambda_s^\alpha} = \frac{1}{d_{grain}} + \sum_{\beta=1}^{N_t} \xi_{\alpha\beta} f^\beta \frac{1}{t(1-f_{tw})} \qquad \text{Eq. 7}$$

where d_{grain} means the average grain size; and $\xi_{\alpha\beta}$ represents the interaction between slip and twin systems (α and β), which includes the coplanar type ($\xi_{\alpha\beta}$=0) and other types ($\xi_{\alpha\beta}$=0.042) [30]. Based on the TEM results on the deformed structures, the average thickness of twin lamellas is 100 × 10^{-9} m. The effect of forest dislocation obstacles on the passing stress τ_b^α in Eq. 4 can be described by Taylor's law as [46]:

$$\tau_b^\alpha = Gb\sqrt{\sum_{\alpha'=1}^{N_s} \xi_{\alpha\alpha'}\rho^{\alpha'}} \qquad \text{Eq. 8}$$

where G is the isotropic shear modulus, $\xi_{\alpha\alpha'}$ accounts for the interaction coefficient between different slip systems, considering self-hardening of 0.122, coplanar of 0.122, collinear of 0.0.625, orthogonal of 0.07, glissile of 0.137, and sessile of 0.122 interactions [47]. According to the Mecking-Kocks model [48], a modification of dislocation density-based evolution rate can be described by:

$$\dot{\rho}^\alpha = \frac{|\dot{\gamma}^\alpha|}{b_s}\left(\frac{1}{k\Lambda_s^\alpha} - 2d_{anni}\rho^\alpha\right) \qquad \text{Eq. 9}$$

where k characterizes the calibration parameter for the Λ_s^α, and d_{anni} is the minimum distance for two dislocations annihilation. The dislocation multiplication can be affected by the dislocation MFP, which is determined by dislocation density, grain size and formation of twins.

2.3.3 Deformation twinning

In addition to dislocation slip, the local plastic deformation can also be attributed to the deformation twins. A shear deformation parallel to the twin planes would be generated [49], and the twin system inducing the shear rate can be given as follows:

$$\dot{\gamma}^\beta = \gamma_{tw}\dot{f}^\beta \qquad \text{Eq. 10}$$

where γ_{tw} presents the twinning shear strain characteristic of $\sqrt{2}/2$ for the FCC structure. The twin fraction change rate can be estimated by [50]:

$$\dot{f}^{\beta} = \left(1 - f_{tw}\right) V^{\beta} \dot{N}_{t}^{\beta} \quad \text{Eq. 11}$$

where V^{β} denotes the volume of newly formed twins, given by

$$V^{\beta} = \frac{\pi}{4} {\Lambda_{t}^{\beta}}^{2} t \quad \text{Eq. 12}$$

where Λ_{t}^{β} is the two obstacles mean spacing affected by deformed twins and is calculated by [30]:

$$\frac{1}{\Lambda_{t}^{\beta}} = \frac{1}{d_{grain}} + \sum_{\beta'=1}^{N_t} \xi_{\beta\beta'} f^{\beta'} \frac{1}{t(1-f_{tw})} \quad \text{Eq. 13}$$

where $\xi_{\beta\beta'}$ is the interaction factor between different twin systems, including coplanar ($\xi_{\beta\beta'} = 0$), non-coplanar ($\xi_{\beta\beta'} = 0.468$) interactions [30].

The $\dot{N}_{t}^{\beta}$ in Eq. 11 means the twin nucleation rate that can be calculated by:

$$\dot{N}_{t}^{\beta} = \dot{N}_{0} p_{ncs} p_{tn} \quad \text{Eq. 14}$$

where $\dot{N}_{0}$ is the reference rate for twin nucleation. The cross-slip can pass away the piled-up dislocations and then relieve the local stress concentration [50], but hinders the interaction between partial dislocations[51]. The comprehensive effect can adversely impact the formation of deformation twinning. Therefore, the probability of non-cross-slip is given by [50]:

$$p_{ncs} = 1 - \exp\left[-\frac{V_{cs}}{k_B T}(\tau_r - \tau^{\beta})\right] \quad \text{Eq. 15}$$

where V_{cs} is the activated volume for dislocation cross-slip which equals to $1.5b^3 = 1.67 \times 10^{-29}\ m^3$, τ^{β} denotes the resolved shear stresses on twin systems and τ_r is the required stress for twin nucleation without external stress by promoting two Shockley partials to the critical distance of $x_c = 1.0 \times 10^{-9}\ m$ [50], which can be expressed as follows:

$$\tau_r = \frac{Gb}{2\pi}\left(\frac{1}{x_0+x_c} + \frac{1}{x_0}\right) \qquad \text{Eq. 16}$$

where x_0 is the equilibrium distance for the two Shockley partials which can be determined by [52]:

$$x_0 = \frac{G}{\Gamma_{sf}}\frac{b^2}{8\pi}\frac{2+v}{1-v} \qquad \text{Eq. 17}$$

where Γ_{sf} and v are SFE and Poisson's ratio, respectively.

The resolved shear stresses of twin systems, τ^{β}, given in Eq. 15, can be calculated as:

$$\tau^{\beta} = \boldsymbol{S}: (\boldsymbol{m}^{\boldsymbol{\beta}} \otimes \boldsymbol{s}^{\alpha}) \qquad \text{Eq. 18}$$

This is the driving force of the deformed twins and can also influence the twin nucleation rate. The probability for formation of the deformation twin can be expressed by:

$$p_{tn} = \exp\left[-\left(\frac{\hat{\tau}_t}{\tau^{\beta}}\right)^{A}\right] \qquad \text{Eq. 19}$$

where $\hat{\tau}_t$ is the twinning critical stres, and A = 8 [31] represents a fitting constant that is used for the description of the sharpness of the transition contours between the non-twinned and twinning statuses [50]. Nucleation of the twins is prone on the GBs and the grain size has a proportional effect on the size of the most easily activated dislocations [53]. Hence, the stress for activating the Frank-Read dislocation source is expressed as [30]:

$$\hat{\tau}_{ds} = \frac{Gb_p}{d_{grain}} \qquad \text{Eq. 20}$$

where $b_p = 0.147\ nm$ (a magnitude of the partials' Burgers vector) [34]. Eq. 20 only involves the nucleation of twins rather than the growth of twins. The twins can grow on the stacking fault (SF), which is related to the separation of partial dislocations. The formation of a wide SF requires critical stress, $\hat{\tau}_{sf}$, which can be described in [30] as:

$$\hat{\tau}_{sf} = \frac{\Gamma_{sf}}{b_p} \quad \text{Eq. 21}$$

Combining these two factors, the critical stress for the deformation twinning is given as follows:

$$\hat{\tau}_t = \hat{\tau}_{ds} + \hat{\tau}_{sf} = \frac{Gb_p}{d_{grain}} + \frac{\Gamma_{sf}}{b_p} \quad \text{Eq. 22}$$

which indicates that the smaller grain size and a higher SFE would have an adverse effect on the formation of a new twin.

3 Results

3.1 Experimental results

3.1.1 Microstructure

Fig. 2 (a_1-a_2) present the EBSD orientation maps from the as-LPBF samples, which are oriented perpendicular to BD. The S1 sample exhibits a combination of columnar-like grains (coarse grains) and equiaxed grains (smaller grains) with a random microstructure and texture. Increasing the laser power to 375W results in the formation of coarsened grains, making the centerline of molten pool more prominent. Hot cracks are absent in those two samples fabricated through varied energy inputs. Within the centerline, fine equiaxed grains were formed without a preferred orientation, while the coarse columnar grains exhibited a <101> // BD texture. Fig. 2 (b_1-b_2) show the EBSD orientation maps on the XY planes of the as-LPBF samples (S1 and S2), fabricated under different parameters. On the XZ surfaces, hierarchical columnar grains with a dominating orientation of <101> and a fiber texture are observed. Although an undetected area is observed as in Fig. 2 b_1, it is important to note that this area is distinct from the prominent hot cracks observed in a previous study on CoCrFeNi [15]. The average grain size from different planes of the S1 and S2 samples is depicted in Fig. 3, illustrating that the increased energy input leads to grain coarsening. Specifically, when the laser powder is increased from 225W to 375W, the average grain size (or grain width) from the XY planes increased from 51.8 μm to 80.2 μm, while the average grain size (or grain length) from the XZ planes is nearly double that of the XY planes.

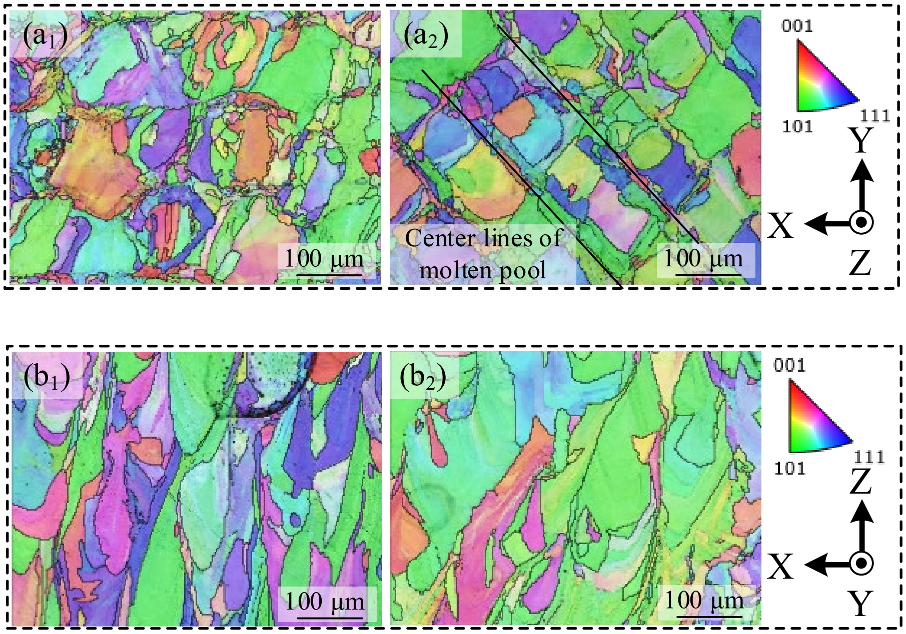

Fig. 2 EBSD orientation maps of XY surfaces (perpendicular to BD) from the as-LPBF sample fabricated with laser power (a_1) 225 W, (a_2) 375 W, respectively with the corresponding orientation maps of XZ surfaces (b_1-b_2)

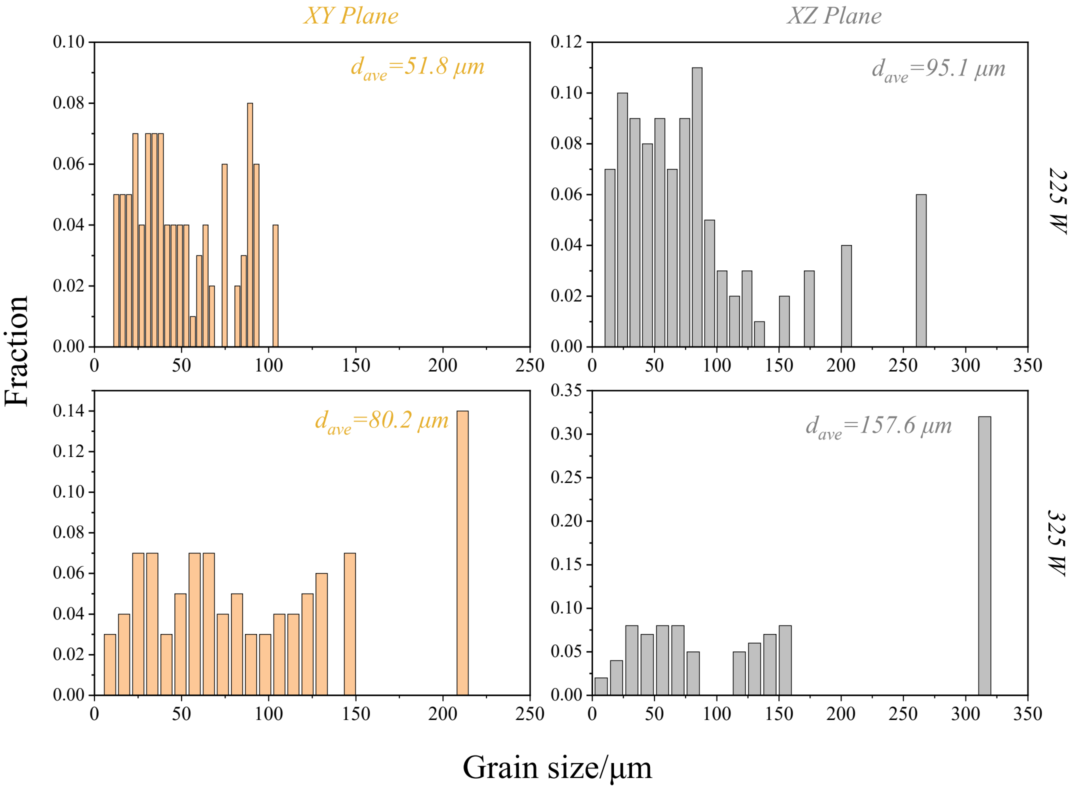

Fig. 3 Grain size charts of different planes from those samples fabricated with the laser power of 225 W and 375 W

3.1.2 Phase and sub-micron microstructure analysis

The XRD profiles of the HEA powder and the as-LPBF sample (S2) on the XY plane are presented in Fig. 4, indicating the presence of FCC structure in both HEA powder and as-LPBF specimen. Fig. 5 provides a sub-micron microstructure of the as-LPBF sample on the plane perpendicular to the BD. Fig. 5 (a) and (b) display EBSD Kernel Average Misorientation (KAM) figure and grain distribution maps of the as-LPBF sample, respectively, revealing the formation of cell structures after LPBF. The KAM map (Fig. 5 (a)) can reflect the strain rate, with green color indicating the presence of large strain in the cell boundary of the as-LPBF samples. The grain boundary distribution map in Fig. 5 (b) illustrates the content of the high-angle and low-angle grain boundaries, demonstrating that low-angle grain boundaries (<15°) were dominant after LPBF resulting in the higher strain in these areas. These findings are quite consistent with the results observed in the as-LPBF pure copper sample [54]. Further investigation of these cell structures was conducted in TEM, as shown in Fig. 5 (c), and they were identified as dislocation networks [22,23,55] due to the large temperature gradient and high growth rate in LPBF [56]. The formation of a dislocation network structure can significantly enhance the mechanical properties of the as-LPBF samples by impeding the dislocation of motion by the dislocation network [19]. Despite the presence of inevitable nano-sized Cr oxides [57], as shown in Fig. 5 (d), and even distribution of alloying elements was observed in the as-LPBF specimen. Additionally, the strengthening effect of formed oxides after the AM procedure was proven to be negligible [58]. Hence, their presence was not considered in the following simulation procedure.

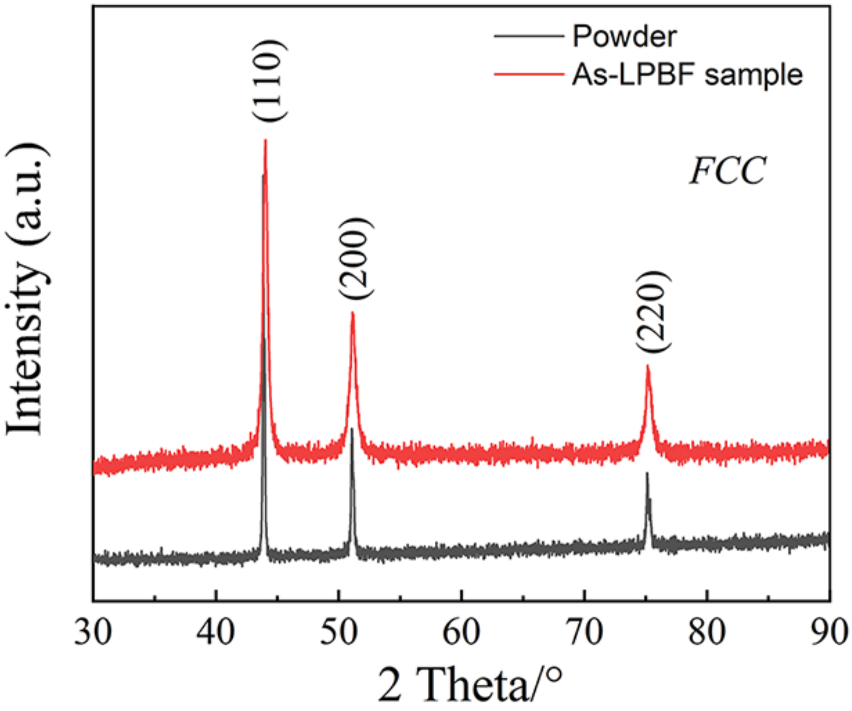

Fig. 4 XRD profiles of HEA power and the as-LPBF sample (S2)

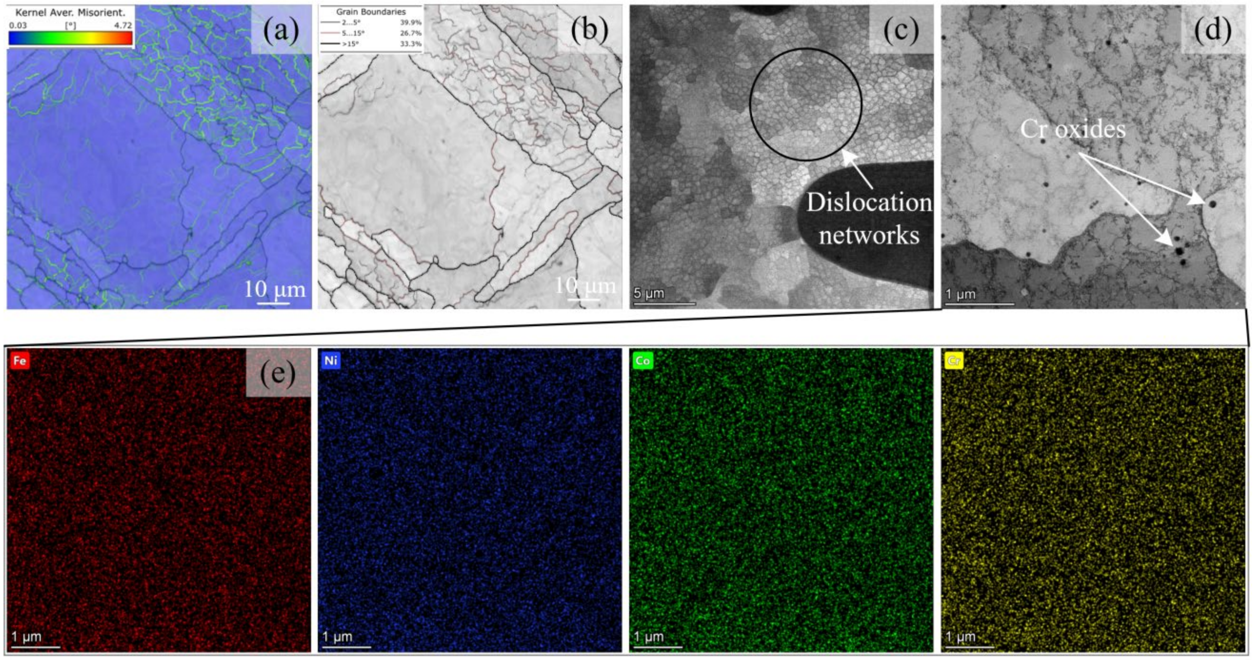

Fig. 5 Microstructure from XY plane in S1 of (a) KAM map and (b) band contrast figure with grain boundary distribution from EBSD (step size of 0.25 μm); (c) and (d) show the dislocation networks captured by TEM under bright field mode with (e) corresponding EDS element maps indicating an even distribution of alloying elements

3.1.3 Mechanical properties and deformation analysis

The typical engineering tensile stress-strain curves from samples fabricated with different laser powers are given in Fig. 6. In this study, the as-LPBF sample fabricated at a laser power of 225 W exhibited superior mechanical properties, including a ultimate tensile strength (UTS) of 707 MPa, yield strength of 535 MPa and a fracture strain of 43.2%. Conversely, the S2 sample (fabricated by 375 W) demonstrated inferior properties compared to S1. This trend can be attributed to the grain boundary strengthening mechanism [59]. According to the Hall-Petch relationship [60], samples fabricated with lower laser input displayed finer grains, resulting in improved and ductility compared to those fabricated with higher laser power. The microstructure evolution in S1 after deformation was investigated using EBSD and TEM, as shown in Fig. 7. The EBSD orientation map obtained from the region near the fracture surface revealed that deformation twins were produced following extensive deformation. The deformed structures were further characterized using Electron Channeling Contrast Imaging (ECCI) and TEM methods, with the selected area electron diffraction (SAED) patterns confirming the presence of deformation twins. Notably, both dislocation slips and deformation twins were prominent during the deformation process [25] in CoCrFeNi HEA.

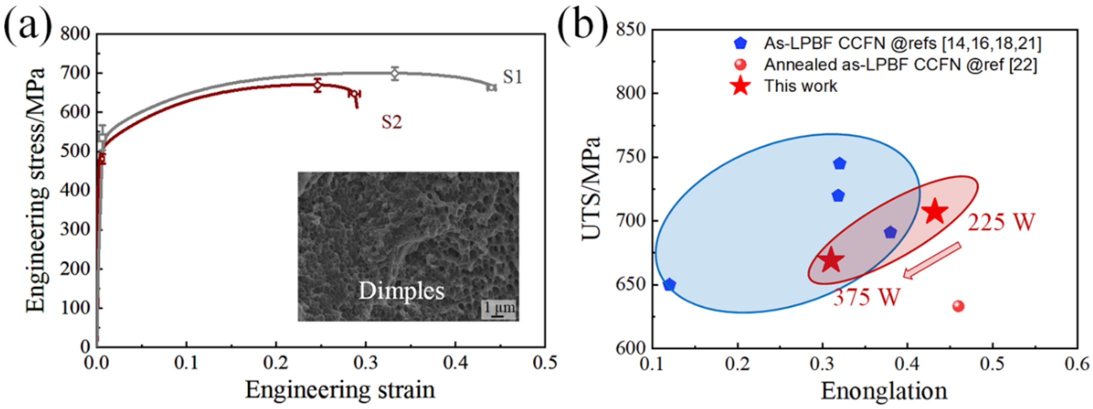

Fig. 6 (a) Typical stress-strain curves from samples fabricated with different laser power inserted with the specific mechanical properties and (b) Ashby plots for the UTS against the elongation of as-LPBF CoCrFeNi HEAs

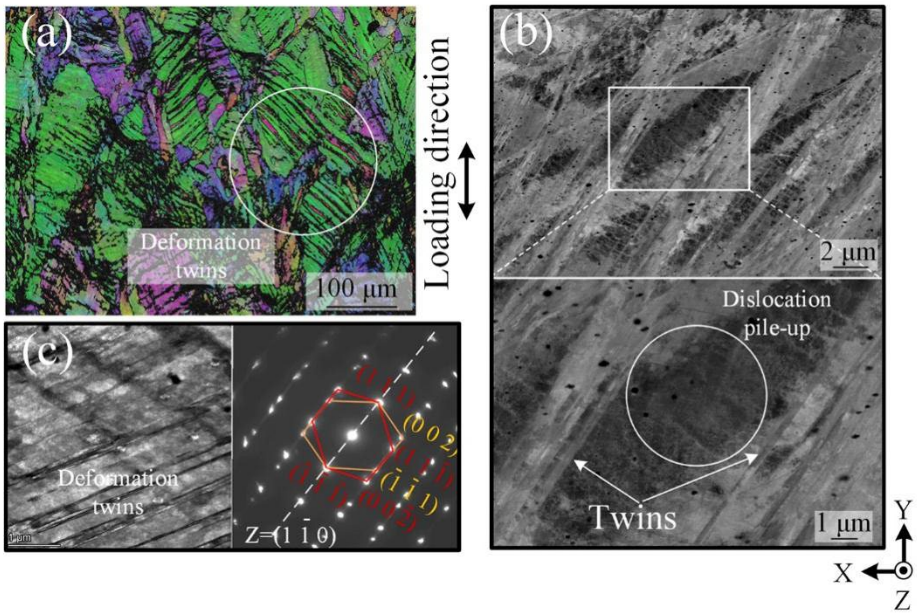

Fig. 7 Microstructure from the near fracture area in S1 of (a) EBSD orientation maps (b) ECC imaging maps and (c) TEM figure showing the formation of deformation twins

3.2 Modelling results

3.2.1 Summary of the modelling framework

The mechanical response of as-LPBF CoCrFeNi HEA during deformation was investigated using the DAMASK (Düsseldorf Advanced Materials Simulation Kit) package, which is based on the dislocation-based crystal plasticity constitutive model [37]. A polycrystalline representative volume element (RVE) was utilized in CPFEM to obtain the parameters in the constitutive model in CPFEM by fitting the tensile curves between experimental and calculated results in sample S1 which exhibited the best properties. Additionally, the constitutive parameters were verified by comparing the modeling and experimental results of sample S2, where the grain size was varied. The RVE, consisting of 27 grains, was meshed into 60 × 60 × 60 elements via Neper utilizing Voronoi tessellations [61] consisting of columnar morphologies with mean aspect ratios of (0.5, 0.5, 1), to maintain the consistency with the EBSD results (Fig. 3) and the simulated models (Fig.

8 (a)). A tensile strain with a rate of 0.001 s^{-1} along X-axis direction was applied in this simulation. The constitutive formulations used in the DAMASK package can accurately reproduce the active deformation models, such as the TWIP phenomenon, in CoCrFeNi HEA, using the specific parameters used in DAMASK. The RVE stress-strain response of the RVE under uniaxial tensile test at a strain rate of 10^{-3}/s along X-axis direction was compared to the experimental results of S1 and S2 samples is depicted in Fig. 8 (b). It can be observed from Fig. 8 (b) that the predicted stress-strain curves, obtained by adjusting the grain size to match the experimental grain size in each sample. Consequently, the constitutive parameters were determined, and all parameters used in CPFEM for CoCrFeNi are provided in Table 1.

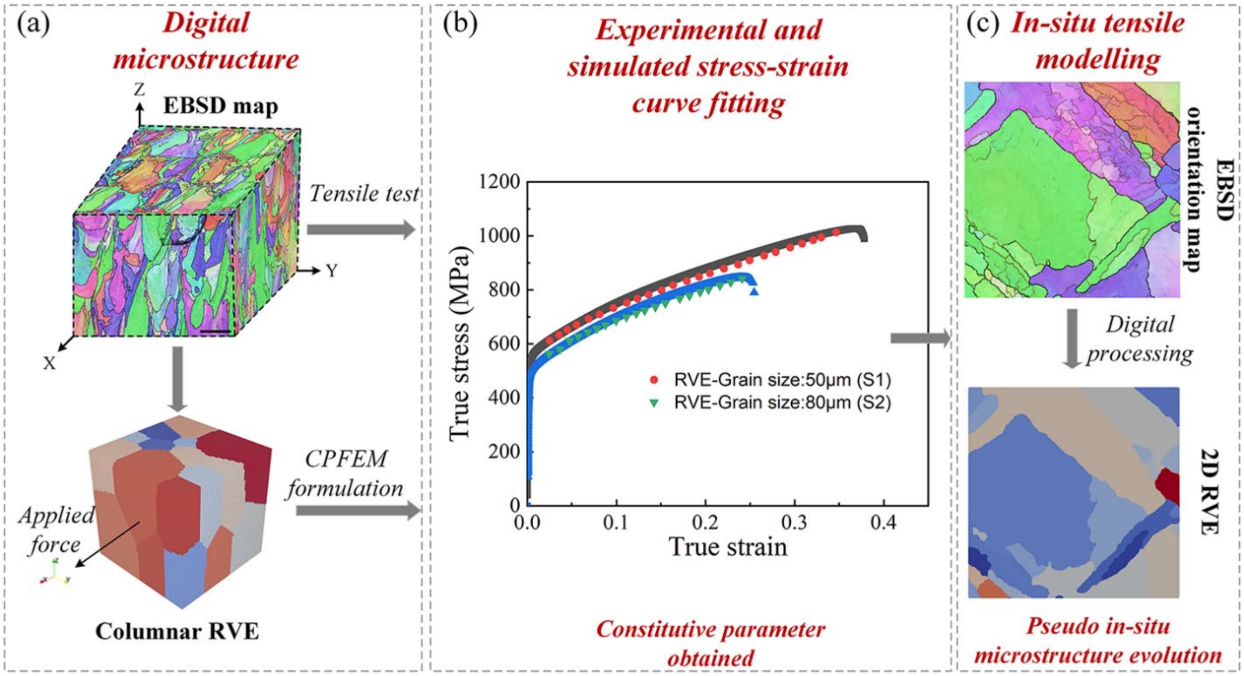

Fig. 8 The CPFEM framework of (a) building columnar RVE with the mean aspect ratios of (0.5, 0.5, 1), (b) obtaining the constitutive parameters by fitting experimental and simulated results and (c) performing the in-situ tensile modeling based on the digital processed EBSD results

Table 1 Material parameters used in the CPFEM for CoCrFeNi HEA

	Symbol	Description	Value
Elastic parameters	C_{11}, C_{12}, C_{44}	Elastic constants	219, 126, 130 GPa [62]
Dislocation glide parameters	b_s	Burgers vector for slipping	2.53×10^{-10} m
	N_{slip}	Total number of slip systems	12
	Q_s	The activation energy for slipping	3.5×10^{-19} J [31]
	Q_c	The activation energy for climbing	3.0×10^{-19} J [31]
	ρ_0^{α}	Initial dislocation density	1×10^{10} m^{-2}
	ρ_{ref}	Reference total dislocation density	2×10^{14} m^{-2}
	p/q	Exponents in slip velocity	1.0/1.15 [34]
	v_0	Reference velocity for slipping	10^{-4} m/s [30]
	i_s	Parameter controlling the dislocation MFP	85
	$\xi_{\alpha\alpha'}$	Interaction coefficients between slip systems	0.122, 0.122, 0.625, 0.07, 0.137, 0.122 [47]
Twinning parameters	b_{tw}	Burgers vector for twinning	1.45×10^{-10} m
	N_{tw}	Total number of twin systems	12
	L_{tw}	Width of twin nucleus	1.8×10^{-7} m
	t_{tw}	Average twin thickness	10×10^{-8} m

V_{cs}	Activation volume for slipping and climbing	$1.5b_s^3$
i_{tw}	The parameter controlling the twin MFP	6
$\xi_{\alpha\beta}$	Interaction coefficients between slip and twin systems	0.0 (coplanar) 0.042 (cross-slip) [30]
$\xi_{\beta\beta'}$	Interaction coefficients between twin systems	0.0 (coplanar) 0.468 (cross-slip) [30]
Γ_{sf}	Stacking fault energy	32.5 mJ/m^2 [24]

3.2.2 In-situ tensile modelling results

The surface morphology parallel to the BD captured by EBSD from the sample S1(see Fig. 5 (a)) was then transformed into a readable format for DMASK using the DREAM.3D software package [36]. The same loading condition was applied to the transformed EBSD results, and the microstructure evolution and fraction of twins at different strain levels were determined (depicted in Fig. 9). At a strain of 3%, the deformed twins began to grow across an entire grain with a specific orientation, as depicted in Fig. 9 (a). As the strain increased, the deformed twins proliferated, as shown in Fig. 9 (b). In addition, at the end of the deformation, not all the grains formed deformed twins insides, illustrating deformed twins would be formed in the grain with preferential grain orientation. To validate the modeling results, an ex-situ EBSD experiment was conducted, and the results, shown in Fig. 9 (c), exhibited a similar trend given by the in-situ CPFEM modelling.

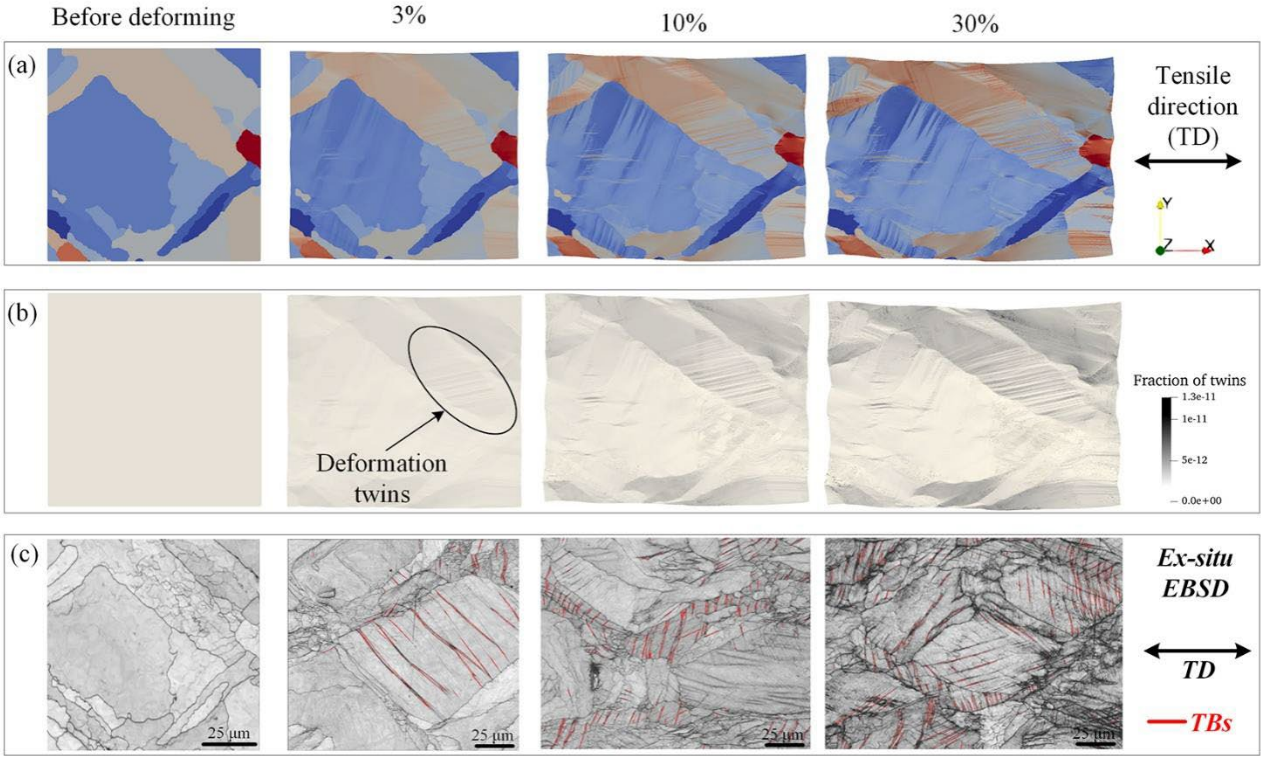

Fig. 9 The microstructure evolution during deformation: (a) orientation maps and (b) fraction of deformed twins from CPFEM results, (c) the verification on the deformed twins by ex-situ EBSD results

Fig. 10 illustrates the evolution of plastic shear strain, the Von Mises strain and stress as strain increases. In Fig. 10 (a), deformation twins start to grow, with the maximum shear strain occurring at the grain boundaries, where twins are prone to nucleate. Barbier et al. [63] found that newly formed twins tend to occur in inferior copper or Gaussian texture rather than changing the grain orientations. In the end, twins form in different grains and the highest shear strain occurs at the grain boundaries, potentially causing misorientation between neighboring grains during the deformation. The Von Mises strain, shown in Fig. 10 (b), increases with the tensile strain, with the maximum strain occurring at the grain boundaries, especially the grain boundary corner. In contrast to the distribution of the Von Mises strain, the maximum Von Mises stress is not only found at the boundaries, including the GBs and TBs, but also within some internal grains. Initially, a strong stress concentration occurs at GBs (see Fig. 10 (c)). As deformation progresses, the stress concentration area expands in various directions within discrete grains, accompanied by the formation of shear bands commonly observed in the ductile alloys and affected by the deformation forms. The dislocation networks form along the shear direction within the shear bands, resulting in uneven strains. In grains with inferior orientation for twin formation, severe dislocation pile-up occurs, leading to high stress within the grain. This implies that grain orientation and loading stress alone cannot reach the critical resolved shear stress (CRSS) required for twinning initiate.

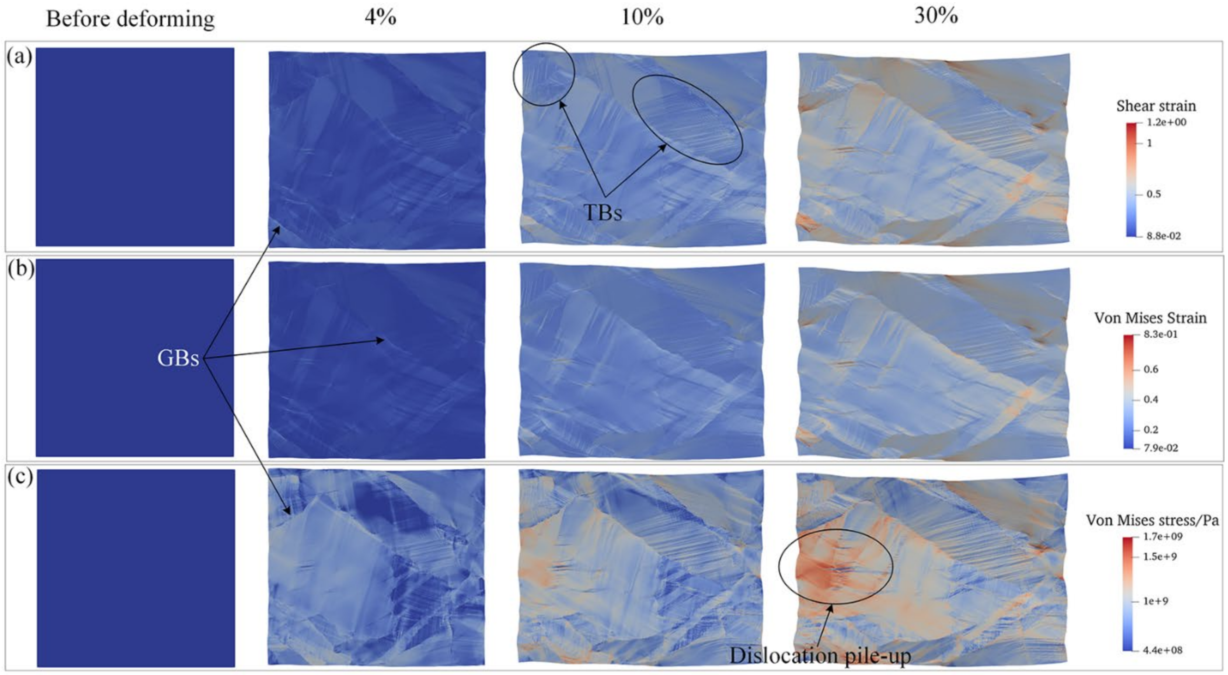

Fig. 10 CPFEM results: (a) the plastic shear stain, (b) Von Mises strain and (c) stress distributions under different strain levels

4 Discussion

4.1 Microstructure evolution after LPBF

After LPBF, columnar grains were observed on XZ plane with a grain size nearly double that of the grains in the XY planes. The traditional theory of solidification, commonly applied in welding or casting, can be used for investigating the solidification process and microstructure evolution, which is guided by the ratio between the temperature gradient (G) and the cooling rate (R) [64]. By decreasing the value of G/R, the solidification modes progress from orderly planar, cellular, columnar to equiaxed dendritic structures [65]. In LPBF, the high cooling rate of 10^6 K/s [65] triggers the growth of cellular structure growth mode to form columnar grains [66]. The largest temperature gradient direction, which aligns with cellular dendritic growth [67], coincides with the normal direction from the boundary to the center of the molten pool. As a result, the increased input energy in LPBF leads to the formation of coarse grains instead of altering the preferred orientations of as-LPBF samples. During the LPBF process, the thermal conductivity is highest along the normal direction to the substrate (the BD direction). Consequently, the columnar grains grow along the BD on the X-Z surfaces for all the samples (Fig. 2) [65]. Increasing the input power density reveals the laser track centerlines, where fine equiaxed grains are obstructed by columnar-like grains, as shown in Fig. 2. During the LPBF process, the temperature gradient (G) at the pool centerline (CL) is lower than that at the fusion line (FL) [68], while the solidification rate (R) exhibits an opposite trend, which makes $(G/R)_{CL} << (G/R)_{FL}$ and causes a transition from the cellular structures to the equiaxed structures [56]. Hence, the equiaxed grains are formed in the centerline of the molten pool.

4.2 Formation mechanism of deformed twins

The SFE would determine the minimum critical shear stress for forming twins. Dislocation slip and the deformation twin are the dominant deformation mechanisms in CoCrFeNi HEA. At different temperatures or strain rates, slip and deformation twins compete with each other. Nevertheless, the latter factor would be dominant during the deformation process, companied with the dislocation movement [69]. The newly formed twins during deformation reduces the MFP of dislocations, increasing the driving force for dislocation slip and promoting the work hardening rate [63,70]. On the other hand, the twin boundaries, formed during deformation, hinder the migration of dislocation slip and promote the local dislocation pile-up [71], regulating deformation between different grains and reducing the likelihood of facture in the as-LPBF CoCrFeNi HEA samples. Additionally, the twinning process during deformation obstructs dislocation slipping in areas of high strain, leading to plasticity induced by dislocation slip in lower-strain areas and extending the development of necking shrinkage[71].

In lower SFE alloys, thicker SFs are easily formed, making it difficult for dislocation co-planar slipping, and prone to producing twins. In general, the critical resolved shear stress (CRSS) for twinning (τ_c^{tw}) is in proportion to the CRSS for slipping (τ_c^{sl}), with a coefficient (m) of 1.65 in Van Houtte's models [72], expressed as:

$$\tau_c^{sl} = \frac{\tau_c^{tw}}{m} \qquad \text{Eq. 23}$$

Sleeswyk and Helle found that the yield stress is determined by the τ_c^{sl}, due to the preferential activation of dislocation slipping to twinning during deformation [73]. This means that dislocation motion is predominant during the elastic stage and the initial plastic deformation stage (strain is less than 3 % in Fig. 10 (a)). During the inceptive plastic deformation stage, dislocation is the only mechanism due to the lower τ_c^{sl} compared to τ_c^{tw}. As the deformation rate increases, the resolved shear stress would increase to τ_c^{tw}, leading to the nucleation and growth of twins. At this stage (with a strain of around 3%), the stress concentration produced on the GBs [63], resulting from uneven deformation formed in polycrystalline materials increases the resolved shear stress to critical value for twinning, satisfying the conditions for forming deformation twins [74,75]. Ovid'ko explained that the nucleation of deformation twins, namely the GB slip and the increase in the driving force for dislocation on GBs, could trigger the relief of partial dislocation on GBs to form deformation twins [76], which is consistent with the shear strain distribution in Fig. 10 (a). The growth of twins is also influenced by the local shear stress concentration on GBs [77]. Additionally, the twin growth is not only determined by the Von Mises stress distribution but also by the preferred grain orientations [78], as shown in Fig. 10 (c), which can increase the resolved shear stress to exceed the CRSS for twinning.

However, the formation of twins can alleviate and increase stress in a complex manner, which is attributed to the interactions between dislocations and twins. The dislocation pile-up formed on TBs can amplify the local stress level (see Fig. 10 (c)), while the dislocation co-planar slip can be produced on TBs by consuming the dislocations and then relieving the local stress. Choi et al. [79] concluded that there are various types of local stress/strain distribution, including the non-twinned grains, twinned grains, and non-twinned/twinned grains, and the highest stress value observed between non-twined and twinned grains. The experimental findings on high Mn steel supported that stress concentration area would result in dislocation file-up and higher local stress [80]. The formation of twins can alleviate stress concentration in certain areas due to the dislocation migration across the TBs to the matrix and the subsequent release of concentrated dislocations [81]. In grains with unfavorable orientations, the initiation of twins necessitates higher stress to surpass the CRSS of twinning. On the other hand, the stress relief on partial twin tips resulting from the shear strain by twin growth, can alter the deformation between twins and the matrix. Furthermore, unmatched deformation between twins and the matrix can facilitate the fracture of CoCrFeNi HEA. In addition, the stress concentration and the local shear defects would lead to fractures in the samples.

5 Conclusions

The CoCrFeNi HEA samples were fabricated using LPBF with varying laser power. The microstructure and mechanical were investigated, and CPFEM was utilized to study the deformation behavior of as-LPBF samples based on the model derived from the experimental results. The main conclusions are as follows:

1) Increasing laser power resulted in the formation of coarser grains in the sample but has little effect on the texture type. The as-LBPF sample exhibited a <101>//BD fiber texture on the planes perpendicular to the BD.

2) At higher energy input, the coarse grains formed in the as-LPBF sample would negatively impact their mechanical properties. The sample manufactured at 225 W exhibited superior properties with a yield strength of 530 ± 31.67 MPa, UTS of 707 ± 16.33 MPa and fracture strain of 43.2 ± 4.3 %. These properties surpass those reported as-LPBF CoCrFeNi specimens.

3) The formation of dislocation networks can significantly increase the yield strength of as-LPBF samples compared to those fabricated using traditional approaches. Additionally, twins formed in the deformation process can hinder the dislocation motion and promote a high ductility.

4) Based on the CPFEM results, the dislocation motion dominates the initial stage of deformation process in the as-LPBF sample. Deformation twins are then prone to nucleate on the grain boundaries with higher shear strains level around 3%. The elevated shear strain during the deformation provides the driving force for the formation of new twins. The interaction between twins and dislocations resulted in complex stress and strain fields, ultimately leading to sample rupture at the end of the deformation stage.

Acknowledgements

The work described in this paper was mainly supported by the funding support to the State Key Laboratories in Hong Kong from the Innovation and Technology Commission (ITC) of the Government of the Hong Kong Special Administrative Region (HKSAR), China. The authors would also like to express their sincere thanks to the financial support from the Research Office (Project code: BBXD and BBX2) of The Hong Kong Polytechnic University, Guangdong Major Project of Basic and Applied Basic Research, China (Grant No. 2019B030302010), the National Key Research and Development Program of China (Grant No. 2021YFA0716302), the National Natural Science Foundation of China (Grant No. 52071222), Guangdong Basic and Applied Basic Research, China (Grant No. 2019B1515130005).

CRediT authorship contribution statement

Y. Zhang: Conceptualization, Methodology, Software, Formal analysis, Data Curation, Writing- Original Dragt, Writing- Review & Editing. **C. Yang**: Methodology, Investigation. **H. Ke**: Conceptualization, Supervision, Writing – review & editing. **K. C. Chan**: Conceptualization, Supervision, Project acquisition, Funding acquisition, Writing – review & editing. **W. Wang**: Conceptualization, Supervision, Funding acquisition. Writing – review & editing.

Conflicts of interest

There authors have no conflicts to declare.

Data availability

The raw/processed data required to reproduce these findings cannot be shared at this time as the data also forms part of an ongoing study.

References

[1] J. Yeh, S. Chen, S. Lin, J. Gan, T. Chin, T. Shun, C. Tsau, Nanostructured High-Entropy Alloys with Multiple Principal Elements : Novel Alloy Design Concepts and Outcomes, Adv. Eng. Mater. 6 (2004) 299–303. https://doi.org/10.1002/adem.200300567.

[2] Z. Li, K.G. Pradeep, Y. Deng, D. Raabe, C.C. Tasan, Metastable high-entropy dual-phase alloys overcome the strength-ductility trade-off, Nature. 534 (2016) 227–230. https://doi.org/10.1038/nature17981.

[3] B. Gorr, M. Azim, H.J. Christ, T. Mueller, D. Schliephake, M. Heilmaier, Phase equilibria, microstructure, and high temperature oxidation resistance of novel refractory high-entropy alloys, J. Alloys Compd. 624 (2015) 270–278. https://doi.org/10.1016/j.jallcom.2014.11.012.

[4] Y.F. Ye, Q. Wang, J. Lu, C.T. Liu, Y. Yang, High-entropy alloy: challenges and prospects, Mater. Today. 19 (2016) 349–362. https://doi.org/10.1016/j.mattod.2015.11.026.

[5] F. He, Z. Wang, Q. Wu, J. Li, J. Wang, C.T. Liu, Phase separation of metastable CoCrFeNi high entropy alloy at intermediate temperatures, Scr. Mater. 126 (2017) 15–19. https://doi.org/10.1016/j.scriptamat.2016.08.008.

[6] W.H. Liu, Z.P. Lu, J.Y. He, J.H. Luan, Z.J. Wang, B. Liu, Y. Liu, M.W. Chen, C.T. Liu, Ductile CoCrFeNiMox high entropy alloys strengthened by hard intermetallic phases, Acta Mater. 116 (2016) 332–342. https://doi.org/10.1016/j.actamat.2016.06.063.

[7] X. Li, Z. Li, Z. Wu, S. Zhao, W. Zhang, H. Bei, Y. Gao, Strengthening in Al-, Mo- or Ti-doped CoCrFeNi high entropy alloys: A parallel comparison, J. Mater. Sci. Technol. 94 (2021) 264–274. https://doi.org/10.1016/j.jmst.2021.02.060.

[8] Y. Cai, L. Zhu, Y. Cui, J. Han, Manufacturing of FeCoCrNi + FeCoCrNiAl laminated high-entropy alloy by laser melting deposition (LMD), Mater. Lett. 289 (2021) 129445. https://doi.org/10.1016/j.matlet.2021.129445.

[9] J. Zhang, K.N. Yoon, M.S. Kim, H.S. Ahn, J.Y. Kim, W.H. Ryu, E.S. Park, Manipulation of microstructure and mechanical properties in N-doped CoCrFeMnNi high-entropy alloys, Metals (Basel). 11 (2021). https://doi.org/10.3390/met11091487.

[10] R.M. Pohan, B. Gwalani, J. Lee, T. Alam, J.Y. Hwang, H.J. Ryu, R. Banerjee, S.H. Hong, Microstructures and mechanical properties of mechanically alloyed and spark plasma sintered

Al0.3CoCrFeMnNi high entropy alloy, Mater. Chem. Phys. 210 (2018) 62–70. https://doi.org/10.1016/j.matchemphys.2017.09.013.

[11] N. Eißmann, B. Klöden, T. Weißgärber, B. Kieback, High-entropy alloy CoCrFeMnNi produced by powder metallurgy, Powder Metall. 60 (2017) 184–197. https://doi.org/10.1080/00325899.2017.1318480.

[12] Y. Zhang, T. Bian, X. Shen, Z. Wang, S. Ye, S. Feng, K. Yu, C. Ding, P. Yu, Sintering mechanism and microstructure evolution of a CoCrFeNiMn high entropy alloy fabricated by metal injection molding, J. Alloys Compd. (2021) 158711.

[13] O.N. Senkov, C.F. Woodward, Microstructure and properties of a refractory NbCrMo0.5Ta0.5TiZr alloy, Mater. Sci. Eng. A. 529 (2011) 311–320. https://doi.org/10.1016/j.msea.2011.09.033.

[14] Y. Brif, M. Thomas, I. Todd, The use of high-entropy alloys in additive manufacturing, Scr. Mater. 99 (2015) 93–96. https://doi.org/10.1016/j.scriptamat.2014.11.037.

[15] Z. Sun, X.P. Tan, M. Descoins, D. Mangelinck, S.B. Tor, C.S. Lim, Revealing hot tearing mechanism for an additively manufactured high-entropy alloy via selective laser melting, Scr. Mater. 168 (2019) 129–133. https://doi.org/10.1016/j.scriptamat.2019.04.036.

[16] D. Lin, L. Xu, Y. Han, Y. Zhang, H. Jing, L. Zhao, F. Minami, Structure and mechanical properties of a FeCoCrNi high-entropy alloy fabricated via selective laser melting, Intermetallics. 127 (2020) 106963. https://doi.org/10.1016/j.intermet.2020.106963.

[17] D. Lin, X. Xi, X. Li, J. Hu, L. Xu, Y. Han, Y. Zhang, L. Zhao, High-temperature mechanical properties of FeCoCrNi high-entropy alloys fabricated via selective laser melting, Mater. Sci. Eng. A. 832 (2022) 142354. https://doi.org/10.1016/j.msea.2021.142354.

[18] Z. Sun, X. Tan, C. Wang, M. Descoins, D. Mangelinck, S.B. Tor, E.A. Jägle, S. Zaefferer, D. Raabe, Reducing hot tearing by grain boundary segregation engineering in additive manufacturing: example of an AlxCoCrFeNi high-entropy alloy, Acta Mater. 204 (2021) 116505. https://doi.org/10.1016/j.actamat.2020.116505.

[19] L. Liu, Q. Ding, Y. Zhong, J. Zou, J. Wu, Y.L. Chiu, J. Li, Z. Zhang, Q. Yu, Z. Shen, Dislocation network in additive manufactured steel breaks strength–ductility trade-off, Mater. Today. 21 (2018) 354–361. https://doi.org/10.1016/j.mattod.2017.11.004.

[20] G.A. Salishchev, M.A. Tikhonovsky, D.G. Shaysultanov, N.D. Stepanov, A. V. Kuznetsov, I. V. Kolodiy, A.S. Tortika, O.N. Senkov, Effect of Mn and v on structure and mechanical properties of high-entropy alloys based on CoCrFeNi system, J. Alloys Compd. 591 (2014) 11–21. https://doi.org/10.1016/j.jallcom.2013.12.210.

[21] Y. Kuzminova, D. Firsov, A. Dudin, S. Sergeev, A. Zhilyaev, A. Dyakov, A. Chupeeva, A. Alekseev, D. Martynov, I. Akhatov, S. Evlashin, The effect of the parameters of the powder bed fusion process on the microstructure and mechanical properties of CrFeCoNi medium-entropy alloys, Intermetallics. 116 (2020) 106651. https://doi.org/10.1016/j.intermet.2019.106651.

[22] D. Lin, L. Xu, H. Jing, Y. Han, L. Zhao, F. Minami, Effects of annealing on the structure and mechanical properties of FeCoCrNi high-entropy alloy fabricated via selective laser melting, Addit. Manuf. 32 (2020) 101058. https://doi.org/10.1016/j.addma.2020.101058.

[23] D. Lin, L. Xu, H. Jing, Y. Han, L. Zhao, Y. Zhang, H. Li, A strong, ductile, high-entropy FeCoCrNi alloy with fine grains fabricated via additive manufacturing and a single cold

deformation and annealing cycle, Addit. Manuf. 36 (2020) 101591. https://doi.org/10.1016/j.addma.2020.101591.

[24] Y. Wang, B. Liu, K. Yan, M. Wang, S. Kabra, Y.L. Chiu, D. Dye, P.D. Lee, Y. Liu, B. Cai, Probing deformation mechanisms of a FeCoCrNi high-entropy alloy at 293 and 77 K using in situ neutron diffraction, Acta Mater. 154 (2018) 79–89. https://doi.org/10.1016/j.actamat.2018.05.013.

[25] A. Pineau, C. Matdriaux, Twinning and strain-induced f.c.c-h.c.p transformation on the mechanical properties of Co-Ni-Cr-Mo alloys, Transformation. 26 (1976) 123–132.

[26] Y.F. Shen, Y.D. Wang, X.P. Liu, X. Sun, R. Lin Peng, S.Y. Zhang, L. Zuo, P.K. Liaw, Deformation mechanisms of a 20Mn TWIP steel investigated by in situ neutron diffraction and TEM, Acta Mater. 61 (2013) 6093–6106. https://doi.org/10.1016/j.actamat.2013.06.051.

[27] B. Qian, J. Zhang, Y. Fu, F. Sun, Y. Wu, J. Cheng, P. Vermaut, F. Prima, In-situ microstructural investigations of the TRIP-to-TWIP evolution in Ti-Mo-Zr alloys as a function of Zr concentration, J. Mater. Sci. Technol. 65 (2021) 228–237. https://doi.org/10.1016/j.jmst.2020.04.078.

[28] Y. Danard, R. Poulain, M. Garcia, R. Guillou, D. Thiaudière, S. Mantri, R. Banerjee, F. Sun, F. Prima, Microstructure design and in-situ investigation of TRIP/TWIP effects in a forged dual-phase Ti–10V–2Fe–3Al alloy, Materialia. 8 (2019) 100507. https://doi.org/10.1016/j.mtla.2019.100507.

[29] M. Diehl, M. Groeber, C. Haase, D.A. Molodov, F. Roters, D. Raabe, Identifying Structure–Property Relationships Through DREAM.3D Representative Volume Elements and DAMASK Crystal Plasticity Simulations: An Integrated Computational Materials Engineering Approach, Jom. 69 (2017) 848–855. https://doi.org/10.1007/s11837-017-2303-0.

[30] X. Lu, J. Zhao, Z. Wang, B. Gan, J. Zhao, G. Kang, X. Zhang, Crystal plasticity finite element analysis of gradient nanostructured TWIP steel, Int. J. Plast. 130 (2020) 102703. https://doi.org/10.1016/j.ijplas.2020.102703.

[31] S.L. Wong, M. Madivala, U. Prahl, F. Roters, D. Raabe, A crystal plasticity model for twinning- and transformation-induced plasticity, Acta Mater. 118 (2016) 140–151. https://doi.org/10.1016/j.actamat.2016.07.032.

[32] Y.Y. Wang, X. Sun, Y.D. Wang, X.H. Hu, H.M. Zbib, A mechanism-based model for deformation twinning in polycrystalline FCC steel, Mater. Sci. Eng. A. 607 (2014) 206–218. https://doi.org/10.1016/j.msea.2014.04.010.

[33] X. Lu, J. Zhao, C. Yu, Z. Li, Q. Kan, G. Kang, X. Zhang, Cyclic plasticity of an interstitial high-entropy alloy: experiments, crystal plasticity modeling, and simulations, J. Mech. Phys. Solids. 142 (2020). https://doi.org/10.1016/j.jmps.2020.103971.

[34] X. Zhang, X. Lu, J. Zhao, Q. Kan, Z. Li, G. Kang, Temperature effect on tensile behavior of an interstitial high entropy alloy: Crystal plasticity modeling, Int. J. Plast. 150 (2022) 103201. https://doi.org/10.1016/j.ijplas.2021.103201.

[35] D. Zhao, H. Fang, T. Jin, T. Zhang, G. Chen, S. Ma, Z. Wang, Constitutive modeling and strain hardening of CoCrFeNiAlx high-entropy alloys, Mater. Res. Express. 6 (2019). https://doi.org/10.1088/2053-1591/ab42e8.

[36] M.A. Groeber, M.A. Jackson, DREAM.3D: A Digital Representation Environment for the Analysis of Microstructure in 3D, Integr. Mater. Manuf. Innov. 3 (2014) 56–72. https://doi.org/10.1186/2193-9772-3-5.

[37] F. Roters, M. Diehl, P. Shanthraj, P. Eisenlohr, C. Reuber, S.L. Wong, T. Maiti, A. Ebrahimi, T. Hochrainer, H.O. Fabritius, S. Nikolov, M. Friák, N. Fujita, N. Grilli, K.G.F. Janssens, N. Jia, P.J.J. Kok, D. Ma, F. Meier, E. Werner, M. Stricker, D. Weygand, D. Raabe, DAMASK – The Düsseldorf Advanced Material Simulation Kit for modeling multi-physics crystal plasticity, thermal, and damage phenomena from the single crystal up to the component scale, Comput. Mater. Sci. 158 (2019) 420–478. https://doi.org/10.1016/j.commatsci.2018.04.030.

[38] X. Song, M. Xie, F. Hofmann, T. Illston, T. Connolley, C. Reinhard, R.C. Atwood, L. Connor, M. Drakopoulos, L. Frampton, A.M. Korsunsky, Residual stresses and microstructure in Powder Bed Direct Laser Deposition (PB DLD) samples, Int. J. Mater. Form. 8 (2015) 245–254. https://doi.org/10.1007/s12289-014-1163-1.

[39] R.J. Asaro, A. Needleman, Overview no. 42 Texture development and strain hardening in rate dependent polycrystals, Acta Metall. 33 (1985) 923–953. https://doi.org/10.1016/0001-6160(85)90188-9.

[40] D. Peirce, R.J. Asaro, A. Needleman, Material rate dependence and localized deformation in crystalline solids, Acta Metall. 31 (1983) 1951–1976. https://doi.org/10.1016/0001-6160(83)90014-7.

[41] R.J. Asaro, J.R. Rice, Strain localization in ductile single crystals, J. Mech. Phys. Solids. 25 (1977) 309–338. https://doi.org/10.1016/0022-5096(77)90001-1.

[42] S.R. Kalidindi, Incorporation of deformation twinning in crystal plasticity models, J. Mech. Phys. Solids. 46 (1998) 267–271. https://doi.org/10.1016/S0022-5096(97)00051-3.

[43] E. Orowan, Problems of plastic gliding, Proc. Phys. Soc. 52 (1940) 8–22. https://doi.org/10.1088/0959-5309/52/1/303.

[44] O. Bouaziz, S. Allain, C. Scott, Effect of grain and twin boundaries on the hardening mechanisms of twinning-induced plasticity steels, Scr. Mater. 58 (2008) 484–487. https://doi.org/10.1016/j.scriptamat.2007.10.050.

[45] C.W. Sinclair, W.J. Poole, Y. Bréchet, A model for the grain size dependent work hardening of copper, Scr. Mater. 55 (2006) 739–742. https://doi.org/10.1016/j.scriptamat.2006.05.018.

[46] G.I. Taylor, Plastic strain in metals, J. Inst. Met. 62 (1938) 307–324.

[47] L. Kubin, B. Devincre, T. Hoc, Modeling dislocation storage rates and mean free paths in face-centered cubic crystals, Acta Mater. 56 (2008) 6040–6049. https://doi.org/10.1016/j.actamat.2008.08.012.

[48] H. Mecking, U.F. Kocks, Kinetics of flow and strain-hardening, Acta Metall. 29 (1981) 1865–1875.

[49] G. Gottstein, Metal Forming (Cold): Dislocation Mechanisms and Microstructural Changes, Encycl. Mater. Sci. Technol. (2001) 5394–5401. https://doi.org/10.1016/b0-08-043152-6/00941-4.

[50] D.R. Steinmetz, T. Jäpel, B. Wietbrock, P. Eisenlohr, I. Gutierrez-Urrutia, A. Saeed-Akbari, T. Hickel, F. Roters, D. Raabe, Revealing the strain-hardening behavior of twinning-induced plasticity steels: Theory, simulations, experiments, Acta Mater. 61 (2013) 494–510. https://doi.org/10.1016/j.actamat.2012.09.064.

[51] S. Kang, J.G. Jung, M. Kang, W. Woo, Y.K. Lee, The effects of grain size on yielding, strain hardening, and mechanical twinning in Fe-18Mn-0.6C-1.5Al twinning-induced plasticity steel, Mater. Sci. Eng. A. 652 (2016) 212–220. https://doi.org/10.1016/j.msea.2015.11.096.

[52] G. Gottstein, Physical foundations of materials science, Springer Science \& Business Media, 2013.

[53] W.Z. Han, Z.F. Zhang, S.D. Wu, S.X. Li, Combined effects of crystallographic orientation, stacking fault energy and grain size on deformation twinning in fcc crystals, Philos. Mag. 88 (2008) 3011–3029. https://doi.org/10.1080/14786430802438168.

[54] G. Wang, H. Ouyang, C. Fan, Q. Guo, Z. Li, W. Yan, Z. Li, The origin of high-density dislocations in additively manufactured metals, Mater. Res. Lett. 8 (2020) 283–290. https://doi.org/10.1080/21663831.2020.1751739.

[55] W. Wu, R. Zhou, B. Wei, S. Ni, Y. Liu, M. Song, Nanosized precipitates and dislocation networks reinforced C-containing CoCrFeNi high-entropy alloy fabricated by selective laser melting, Mater. Charact. 144 (2018) 605–610. https://doi.org/10.1016/j.matchar.2018.08.019.

[56] S. Kou, Welding metallurgy, New Jersey, USA. 431 (2003) 223–225.

[57] M. Song, R. Zhou, J. Gu, Z. Wang, S. Ni, Y. Liu, Nitrogen induced heterogeneous structures overcome strength-ductility trade-off in an additively manufactured high-entropy alloy, Appl. Mater. Today. 18 (2020) 1–6. https://doi.org/10.1016/j.apmt.2019.100498.

[58] Y.M. Wang, T. Voisin, J.T. McKeown, J. Ye, N.P. Calta, Z. Li, Z. Zeng, Y. Zhang, W. Chen, T.T. Roehling, R.T. Ott, M.K. Santala, P.J. Depond, M.J. Matthews, A. V. Hamza, T. Zhu, Additively manufactured hierarchical stainless steels with high strength and ductility, Nat. Mater. 17 (2018) 63–70. https://doi.org/10.1038/NMAT5021.

[59] Z.G. Zhu, X.H. An, W.J. Lu, Z.M. Li, F.L. Ng, X.Z. Liao, U. Ramamurty, S.M.L. Nai, J. Wei, Selective laser melting enabling the hierarchically heterogeneous microstructure and excellent mechanical properties in an interstitial solute strengthened high entropy alloy, Mater. Res. Lett. 7 (2019) 453–459. https://doi.org/10.1080/21663831.2019.1650131.

[60] C.T. Liu, C.L. White, J.A. Horton, Effect of boron on grain-boundaries in Ni3Al†, Acta Metall. 33 (1985) 213–229. https://doi.org/10.1016/0001-6160(85)90139-7.

[61] R. Quey, P.R. Dawson, F. Barbe, Large-scale 3D random polycrystals for the finite element method: Generation, meshing and remeshing, Comput. Methods Appl. Mech. Eng. 200 (2011) 1729–1745. https://doi.org/10.1016/j.cma.2011.01.002.

[62] B. Yin, W.A. Curtin, Origin of high strength in the CoCrFeNiPd high-entropy alloy, Mater. Res. Lett. 8 (2020) 209–215. https://doi.org/10.1080/21663831.2020.1739156.

[63] D. Barbier, N. Gey, S. Allain, N. Bozzolo, M. Humbert, Analysis of the tensile behavior of a TWIP steel based on the texture and microstructure evolutions, Mater. Sci. Eng. A. 500 (2009) 196–206. https://doi.org/10.1016/j.msea.2008.09.031.

[64] T. Niendorf, S. Leuders, A. Riemer, H.A. Richard, T. Tröster, D. Schwarze, Highly anisotropic steel processed by selective laser melting, Metall. Mater. Trans. B Process Metall. Mater. Process. Sci. 44 (2013) 794–796. https://doi.org/10.1007/s11663-013-9875-z.

[65] H.Y. Wan, Z.J. Zhou, C.P. Li, G.F. Chen, G.P. Zhang, Effect of scanning strategy on grain structure and crystallographic texture of Inconel 718 processed by selective laser melting, J. Mater. Sci. Technol. 34 (2018) 1799–1804. https://doi.org/10.1016/j.jmst.2018.02.002.

[66] D. Wang, C. Song, Y. Yang, Y. Bai, Investigation of crystal growth mechanism during selective laser melting and mechanical property characterization of 316L stainless steel parts, Mater. Des. 100 (2016) 291–299. https://doi.org/10.1016/j.matdes.2016.03.111.

[67] B. Vrancken, L. Thijs, J.P. Kruth, J. Van Humbeeck, Microstructure and mechanical properties of a novel β titanium metallic composite by selective laser melting, Acta Mater. 68 (2014) 150–158. https://doi.org/10.1016/j.actamat.2014.01.018.

[68] R. Shi, S.A. Khairallah, T.T. Roehling, T.W. Heo, J.T. McKeown, M.J. Matthews, Microstructural control in metal laser powder bed fusion additive manufacturing using laser beam shaping strategy, Acta Mater. 184 (2020) 284–305.

[69] S. Curtze, V.T. Kuokkala, Dependence of tensile deformation behavior of TWIP steels on stacking fault energy, temperature and strain rate, Acta Mater. 58 (2010) 5129–5141. https://doi.org/10.1016/j.actamat.2010.05.049.

[70] C. Efstathiou, H. Sehitoglu, Strain hardening and heterogeneous deformation during twinning in Hadfield steel, Acta Mater. 58 (2010) 1479–1488. https://doi.org/10.1016/j.actamat.2009.10.054.

[71] F. Shen, J. Zhou, Y. Liu, R. Zhu, S. Zhang, Y. Wang, Deformation twinning mechanism and its effects on the mechanical behaviors of ultrafine grained and nanocrystalline copper, Comput. Mater. Sci. 49 (2010) 226–235. https://doi.org/10.1016/j.commatsci.2010.04.044.

[72] P. Van Houtte, Simulation of the rolling and shear texture of brass by the Taylor theory adapted for mechanical twinning, Acta Metall. 26 (1978) 591–604. https://doi.org/10.1016/0001-6160(78)90111-6.

[73] A.W. Sleeswykt, Ductile cleavage fracture, yielding and twinning in a-iron, Acta Metall. 11 (1963) 187–194.

[74] R.Y. Zhang, M.R. Daymond, R.A. Holt, A finite element model of deformation twinning in zirconium, Mater. Sci. Eng. A. 473 (2008) 139–146. https://doi.org/10.1016/j.msea.2007.04.021.

[75] H.R. Wenk, C. Janssen, T. Kenkmann, G. Dresen, Mechanical twinning in quartz: Shock experiments, impact, pseudotachylites and fault breccias, Tectonophysics. 510 (2011) 69–79. https://doi.org/10.1016/j.tecto.2011.06.016.

[76] I.A. Ovid'Ko, N. V. Skiba, Nanotwins induced by grain boundary deformation processes in nanomaterials, Scr. Mater. 71 (2014) 33–36. https://doi.org/10.1016/j.scriptamat.2013.09.028.

[77] I. Gutierrez-Urrutia, S. Zaefferer, D. Raabe, The effect of grain size and grain orientation on deformation twinning in a Fe-22wt.% Mn-0.6wt.% C TWIP steel, Mater. Sci. Eng. A. 527 (2010) 3552–3560. https://doi.org/10.1016/j.msea.2010.02.041.

[78] P. Thamburaja, H. Pan, F.S. Chau, The evolution of microstructure during twinning: Constitutive equations, finite-element simulations and experimental verification, Int. J. Plast. 25 (2009) 2141–2168. https://doi.org/10.1016/j.ijplas.2009.02.004.

[79] S.H. Choi, D.H. Kim, S.S. Park, B.S. You, Simulation of stress concentration in Mg alloys using the crystal plasticity finite element method, Acta Mater. 58 (2010) 320–329. https://doi.org/10.1016/j.actamat.2009.09.010.

[80] I. Karaman, H. Sehitoglu, K. Gall, Y.I. Chumlyakov, H.J. Maier, Deformation of single crystal hadfield steel by twinning and slip, Acta Mater. 48 (2000) 1345–1359. https://doi.org/10.1016/S1359-6454(99)00383-3.

[81] S.G. Song, G.T. Gray, Influence of temperature and strain rate on slip and twinning behavior of zr, Metall. Mater. Trans. A. 26 (1995) 2665–2675. https://doi.org/10.1007/BF02669423.